JOURNAL OF SPACECRAFT AND ROCKETS
Vol. 33, No. 4, July–August 1996

Ion-Thruster Plume Modeling for Backflow Contamination

R. I. Samanta Roy* and D. E. Hastings†
Massachusetts Institute of Technology, Cambridge, Massachusetts 02139
and
N. A. Gatsonis‡
Worcester Polytechnic Institute, Worcester, Massachusetts 01609

An axisymmetric model of the plume and backflow contamination from an ion-thruster plume is presented. Components included are primary beam ions, neutral propellant efflux, thermal propellant ions created mainly by charge-exchange collisions between primary beam ions and neutral propellant, nonpropellant efflux sputtered from thruster components, and neutralizing electrons. The plasma hybrid particle-in-cell technique is applied to both propellant charge-exchange ions and nonpropellant efflux ions produced within the beam and to their transport out of the beam to the regions surrounding a model spacecraft. Simulation results for plume properties such as ion density, beam potential, and ion flow angle are compared with experimental data. It is shown that the charge-exchange ions formed in the beam are accelerated outward by strong radial beam electric fields and form two distinct energy populations—one with a significant backstreaming velocity component.

Nomenclature

A_g = sputtered grid area, m^2
A_n = grid neutral flow through area, m^2
$\boldsymbol{B}$ = fixed ambient magnetic field, T
$\bar{C}$ = neutral average speed, m/s
$\boldsymbol{E}$ = electric field, V/m
$E_{\rm mp}$ = most probable sputtering energy, eV
e = electron charge, C
I_b = thruster beam ion current (superscripts ++ and + denote doubly and singly charged ions), A
$j_{bi,e}$ = beam ion, electron current density, A/m^2
k = Boltzmann's constant (mks)
L = characteristic length for changes in electron drift velocity (on the order of the beam radius), m
$\mathcal{M}$ = molecular weight, kg/mole
$m_{e,i}$ = electron, ion mass, kg
$\dot{m}_T$ = thruster total mass flow rate, kg/s
$\dot{N}$ = charge-exchange ion production rate, m^{-3} s^{-1}
$\mathcal{N}_A$ = Avogadro's number
n_{bi} = beam ion density, m^{-3}
$n_{i,e,n}$ = total ion, electron, neutral density, m^{-3} (a further subscript 0 denotes reference)
p_e = electron pressure, N/m^2
Q_e = electron heating–cooling term, W/m^3
q/m = charge-to-mass ratio of ions, C/kg
R_c = radius of curvature of grids, m
$\boldsymbol{R}_e$ = electron collisional drag term, m/s^2
r_T = thruster radius, m
$T_{e,i}$ = electron, ion temperature, K
T_{e0} = beam electron temperature, K
T_w = thermal wall temperature of neutrals, K
V = characteristic electron drift velocity, m/s
$v_{bi,e}$ = beam-ion, electron drift velocity, m/s
$v_{te,ti}$ = electron, ion thermal velocity, m/s
α = beam divergence angle, rad
Γ_s = sputtered grid material flux, m^{-2} s^{-1}
η^{++} = doubly charged ion correction factor
η_p = propellant utilization efficiency
κ_e = electron thermal conductivity, W/m K
Λ = Coulomb logarithm
$\nu_{ei,en,e}$ = e–ion, e–neutral, total electron collision frequency, s^{-1}
$\sigma_{\rm cex}$ = charge-exchange cross section, m^2
σ_{en} = electron–neutral elastic cross section, m^2
τ = characteristic time scale for changes in characteristic electron drift velocity, s
Φ_b = beam acceleration voltage, V
ϕ = electric potential, V
ω_{ce} = electron cyclotron frequency, rad/s

Received May 23, 1995; revision received Feb. 15, 1996; accepted for publication Feb. 16, 1996.

*Postdoctoral Associate, Space Power and Propulsion Laboratory, Department of Aeronautics and Astronautics; currently Research Staff Member, Institute for Defense Analyses, Alexandria, VA 22311. Member AIAA.
†Professor, Space Power and Propulsion Laboratory, Department of Aeronautics and Astronautics. Associate Fellow AIAA.
‡Assistant Professor, Mechanical Engineering Department. Member AIAA.

Introduction

ELECTRIC propulsion (EP) is increasingly being considered earnestly for a variety of applications ranging from technology demonstrators to science missions and commercial applications such as stationkeeping on geostationary communications satellites.[1] The advantage of the high exhaust velocities of EP thrusters in mass savings is significant compared to chemical propulsion. However, in addition to increased propulsion-system performance, spacecraft designers and integrators must also consider the unique and important issues of spacecraft contamination by EP thruster plume backflow, and how EP thrusters modify the environment surrounding a spacecraft. Spacecraft contamination is also an important issue for chemical rockets. However, the induced environment in the vicinity of an EP spacecraft is unique, consisting of neutral gases, plasmas, and electromagnetic fields as a result of interactions between the ambient environment, the thruster effluents, and the spacecraft itself. In comparison with chemical propulsion environments, which primarily consist of neutral gases, the plasma plume generated by EP thrusters introduces new complexity into the spacecraft interaction picture.

The evaluation of EP-thruster-induced environmental effects that could degrade the performance of spacecraft subsystems and sensors is very important. For example, in some thruster plumes, a low-energy plasma is created by charge-exchange (CEX) collisions and can expand around a spacecraft. Many thrusters also emit heavy-metal species, both charged and uncharged, due to thruster component erosion. These thruster effluents, in addition to other neutral and plasma species, contribute to the induced environment surrounding a spacecraft and can lead to, or influence, various interactions, such as parasitic current flows to biased surfaces; degradation of solar-array panels, thermal control surfaces, and optical windows due to effluent deposition; attenuation and refraction of electromagnetic-wave transmission and reception due to enhanced plasma density;

absolute and differential charging of the spacecraft; interference due to electromagnetic noise; and the alteration of electrical and thermal properties of surfaces.[2] Most of these interactions are detrimental to spacecraft operation, and surface contamination in particular can seriously degrade spacecraft performance and decrease the operational lifetime.

A review of the literature regarding interactions of EP-thruster spacecraft reveals an awareness of many of the above issues from early in the development of EP thrusters.[2,3] However, accurate measurement and prediction of thruster effluents were hampered by both experimental and numerical limitations. As a result of experimental-facility effects, many ground results are questionable,[4] and only recently has the computational power been available for the development of rigorous numerical models of thruster plumes. Historically, much effort in the United States has focused on the development of ion thrusters. Hence, the issues of ion-thruster contamination have received the most attention, and a large plume database exists, although most of it was taken when mercury was used as a propellant. (Currently, xenon is the most common propellant.) The thruster effluents were characterized, and efforts were made to develop simple models of contaminating fluxes. In addition, a number of computational models were developed,[5,6] but they possess many shortcomings in view of their numerous assumptions.[7] Currently, no comprehensive model exists that can predict, in a self-consistent manner, the charged-particle backflow from an ion-thruster plume. The need for such a capability is the motivation for this work.

The model presented addresses two important issues dealing with ion-thruster backflow. One such issue is that complete ionization is not achieved with reasonable levels of power, and hence, neutral propellant is emitted at thermal speeds. We are interested in these slow neutrals because they undergo CEX collisions with the fast beam ions, producing fast neutrals and slow ions, of which the latter can be influenced by local electric fields in the plume. Slow ions can also be produced by electron impact ionization if the electron temperature is sufficiently high, but CEX is generally the dominant collisional process. The electric field structure in the plume, as seen in experiments, is radial, and hence the slow propellant ions are pushed out of the beam and move back towards the spacecraft. These ions, typically xenon, do not pose a serious contamination hazard unless spacecraft surfaces are extremely cold. However, these xenon ions can present a current flow to biased surfaces.

More important is the second issue: that the grids of ion thrusters are bombarded by some of these propellant CEX ions, causing erosion. Hence, molybdenum, a common grid material, is sputtered into the plume. A fraction of the sputtered grid atoms becomes charged and flows back towards the spacecraft, creating a potentially serious contamination hazard due to the low vapor pressure of these metals. For spacecraft designers and integrators, it is important to have models for plume backflow and to understand how these contaminating species behave as a function of thruster operating conditions. In this paper, we present the theory of the model and show comparisons with data. In a companion paper,[8] we apply the model to conduct a study of backflow contamination and other interactions of a modern xenon ion thruster.

Physical Model

The plumes of ion thrusters contain a number of major components: 1) fast (>10 km/s) propellant beam ions that provide the thrust, 2) un-ionized propellant neutrals that escape from both the discharge chamber and the neutralizer, 3) slow (initially thermal) propellant ions created predominantly from CEX collisions between the beam ions and neutrals, 4) nonpropellant efflux (NPE) that consists mainly of eroded grid material, typically molybdenum, and 5) electrons. We will consider each of these species below. The focus of our model is the production of ions primarily due to CEX collisions within the beam, and their transport outward. Since the CEX ion creation rates for both the propellant and NPE ions depend on the beam ion and the various neutral densities, models for these density fields are necessary.

Beam Ions

The primary ion thruster effluent is the directed energetic singly charged ions in the beam that are accelerated by the thruster grids

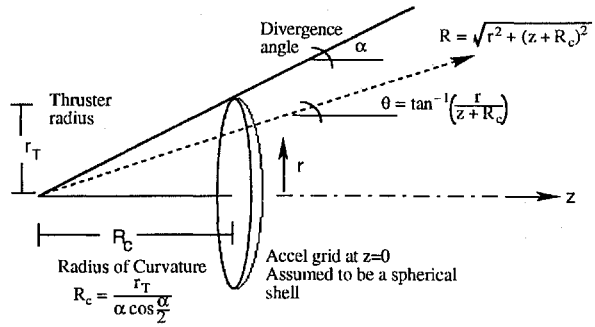

Fig. 1 Geometry of ion beam.

through voltage drops of around 1 kV or more and follow nearly line-of-sight trajectories. Experimentally, it is found that most of these ions lie within an expansion cone of half angle 15–20 deg. The beam divergence is primarily due to the fringe electric fields in the grid holes that defocus the ions, and to the curvature of the grids.

For this study, we take the thruster grid to be a spherical segment (convex side downstream), with the velocities of the beam ions normal to the surface. Hence, the ions appear to be leaving a point source located at a distance R_c (the radius of curvature of the grids) behind the thruster exit plane. The radius of curvature is given in terms of the thruster beam radius r_T and beam divergence angle α by $R_c = r_T/[\alpha \cos(\alpha/2)]$. Figure 1 displays the geometry. The velocity of the singly charged beam ions of mass m_i is expressed as $v_{bi} = (2e\Phi_b/m_i)^{1/2}$, where Φ_b is the beam potential. Over length scales of interest (<2–5 m), the beam ion velocities are assumed to be constant throughout the beam.

The radial current density profile of the collimated beam ions [given in spherical polar coordinates (R, θ) for simplicity] is taken to be approximated by a parabolic axisymmetric profile given by

$$j_{bi}(R, \theta) = ev_{bi}A(R_c/R)^2[1 - (\theta^2/\alpha^2)] \tag{1}$$

which is subject to the normalization imposed by continuity at any downstream location in the beam,

$$I_b = \int_0^{\alpha} j_{bi} 2\pi R^2 \sin\theta \, d\theta \tag{2}$$

The normalization constant A, which is the centerline beam ion density at the thruster exit, is given by

$$A = n_{bi0} = \frac{I_b}{2\pi R_c^2 e v_{bi} \delta} \tag{3}$$

where δ is

$$\delta = 1 - \frac{2\cos\alpha}{\alpha^2} - \frac{2\sin\alpha}{\alpha} + \frac{2}{\alpha^2} \tag{4}$$

Previous beam models[5] have utilized a parabolic core and an exponential wing. Since the parabolic profile drops sharply to zero at the beam edge, we adopt this approach and hold Eq. (1) valid for $\theta \leq \zeta\alpha$, whereas for $\theta \geq \zeta\alpha$, the current density is attenuated by a factor $\exp(-r/\lambda)$. Typically, ζ is taken to be 0.95, and λ is a decay length scale that is a fraction of the beam radius. Since this smoothing region is small and the densities are small, we neglect the current-density contribution in the calculation of the normalization constant in Eq. (2). Given the beam ion current density, the beam ion density is then determined by

$$n_{bi}(r, z) = \frac{j_{bi}(r, z)}{ev_{bi}} \tag{5}$$

Early-generation ion thrusters often had much more peaked radial ion density profiles.[9] To model these thrusters, a Gaussian profile fits measured density profiles better than parabolic shapes. For these thrusters, we take the beam ion current density to be given by

$$j_{bi}(r, z) = \frac{I_b}{\xi^2 \pi r_b^2} \exp\left[-\left(\frac{r}{\xi r_b}\right)^2\right] \tag{6}$$

where $r_b = r_T + z\tan\alpha$ and ξ is a scaling factor for the Gaussian half-width.

In the discharge chambers of ion thrusters, a fraction of doubly charged ions is produced. Because of their increased charge, these ions are unfocused in the grids and leave at large angles, decreasing the overall thrust efficiency. In ion-thruster performance tests, a correction factor due to the doubly charged ions is defined as the ratio of the sum of the thrusts from both singly and doubly charged ions to the thrust if all ions were singly charged. This thrust ratio can be expressed as

$$\eta^{++} = \frac{1 + (1/\sqrt{2})\left(I_b^{++}/I_b^{+}\right)}{1 + \left(I_b^{++}/I_b^{+}\right)} \tag{7}$$

For a typical modern 30-cm xenon thruster, η^{++} varies from 0.995 at $I_b = I_b^{+} + I_b^{++} = 1.45$ A to 0.956 at $I_b = 5$ A (Ref. 10). Therefore, the ratios of doubly to singly charged ion density are 0.006 and 0.063, respectively. Because their population is small compared to the singly charged ions, and their CEX probability is also very low, we will neglect the role of any doubly charged propellant ions in the beam.

Neutral Model

Not all the propellant is ionized in the discharge chamber of ion thrusters, on account of chamber inefficiencies and operating constraints. The propellant utilization efficiency η_p is defined as the ratio of the beam ion current to the total propellant mass flow rate $\dot{m}_T$,

$$\eta_p = (I_b/\dot{m}_T)(m_i/e) \tag{8}$$

Typical propellant utilization efficiencies range from 0.7 to 0.95.

The un-ionized propellant effuses out from the discharge chamber, and exits through the grids in free-molecular flow with a temperature close to that of the discharge-chamber walls. Typically, this temperature is around 500 K for thrusters using xenon. Because of the hole structure, the grids have a transparency that is close to the ratio of the area through which neutrals can leak out to the total geometric area. This value is typically 0.1–0.3. Whereas the overall flow is quite complicated, the flow from each individual hole is given by the Knudsen efflux, $n_{n0}\bar{C}/4$, where $\bar{C}$ is the mean thermal speed given by $(8kT_w/\pi m_i)^{1/2}$. Far from the grids, the fine structure of the holes decays, and the neutral flow can be regarded as the superposition of a large number of point sources. The average neutral density right at the thruster grids can be determined from the beam ion current and the total propellant utilization efficiency by the relation

$$n_{n0} = \frac{4I_b}{e\bar{C}A_n}\left(\frac{1-\eta_p}{\eta_p}\right) \tag{9}$$

Even with high utilization fractions, neutral densities are higher than ion densities, since the velocity of the neutral atoms is much lower than that of the ions. For example, the ion and neutral densities at the exit of a 30-cm ($r_T = 0.15$ m) xenon ion thruster with a beam divergence angle of 20 deg operating with a specific impulse of 3477 s ($v_{bi} = 40{,}200$ m/s), $I_b = 1.74$ A with neutrals at 500 K, $\eta_p = 0.89$, and a grid transparency fraction of 0.24, are $n_{bi0} = 7.5 \times 10^{15}$ m^{-3} and $n_{n0} = 1.1 \times 10^{18}$ m^{-3}.

In this work, the neutral density field is modeled as the flow from a single-point source that is located one thruster radius behind the exit plane of the grids. For a neutral gas of density n_{n0} effusing from a source located one beam radius (r_T) behind the thruster exit, the density in spherical polar coordinates is given by[11]

$$n_n(R,\theta) = a(n_{n0}/2)\left\{1 - \left[1 + (r_T/R)^2\right]^{-\frac{1}{2}}\right\}\cos\theta \tag{10}$$

where $a = (1-1/\sqrt{2})^{-1}$ is a correction factor to allow for the shifting of the point source and $R = [r^2 + (z + r_T)^2]^{1/2}$, $\theta = \tan^{-1}[r/(z + r_T)]$.

The effect of the neutrals from the neutralizer is incorporated into the neutral density by using the total mass flow rate. The actual neutral density flowfield will be affected by the presence of the neutralizer off the beam axis, and will dep .d on its location and operational characteristics. However, such perturbations on the structure of the neutral flowfield are neglected.

During ground tests, there is a finite background neutral density that resides in the vacuum tanks. Many test chambers of meter-size class can not achieve a pressure below 10^{-6}–10^{-5} torr (10^{-4}–10^{-3} Pa). This results in a residual background density of around 3×10^{16}–3×10^{17} m^{-3}, which can be comparable to the neutral density in the thruster plume. From the plume modeling perspective, the background gas is an important factor that must be included when comparing simulation results with ground-test data, since the background gas increases the CEX ion production rates. In addition, the velocity characteristics of the background neutrals are different from those of the neutrals coming from the thruster. The temperature of the facility neutrals is less, and the velocity distribution is isotropic. In comparison, the thruster neutrals are hotter, and their velocities are oriented downstream (they are flowing away from the thruster). These velocity differences are important in that the behavior of the CEX plasma in ground-based tests will be different from that which will be observed in space.

Lastly, there are neutrals in the plume that are created from the CEX processes. These neutrals, formerly beam ions, possess the beam ion velocity and leave the vicinity of the spacecraft rapidly. Their density is that of the CEX ion density, which we will see is orders of magnitude less than the beam neutral density. Thus, the contribution of this component to the total propellant neutral density can be neglected.

CEX Propellant Ions

Slow propellant ions are created, both within the thruster grids and downstream inside the beam, by resonant CEX collisions of the following type between the fast beam ions and the slow thermal neutrals (e.g., for xenon):

$$\mathrm{Xe}^{+}_{\mathrm{fast}} + \mathrm{Xe}^{0}_{\mathrm{slow}} \rightarrow \mathrm{Xe}^{+}_{\mathrm{slow}} + \mathrm{Xe}^{0}_{\mathrm{fast}} \tag{11}$$

The result is a fast neutral that travels in a line of sight, and a slow ion that is affected by the strong radial electric fields in the beam. The CEX ions created can be classified according to the regions wherein they were born.[12,13] We are most interested in the CEX ions created directly downstream of the thruster exit, because they are the dominant component of the backflow.

The spatial volumetric production rate of CEX ions is given by

$$\dot{N}_{\mathrm{cex}}(\boldsymbol{x}) = n_n(\boldsymbol{x})n_{bi}(\boldsymbol{x})v_{bi}\sigma_{\mathrm{cex}}(v_{bi}) \tag{12}$$

where the relative collision velocity is taken to be the beam ion velocity. Based on theory, which is in good agreement with available data, the velocity-dependent resonant CEX cross section in square meters as a function of the beam ion velocity in meters per second can be expressed as[14]

$$\sigma_{\mathrm{cex}} = (k_1 \ell_n v_{bi} + k_2)^2 \times 10^{-20}\,\mathrm{m}^2 \tag{13}$$

For xenon, $k_1 = -0.8821$ and $k_2 = 15.1262$; for mercury, $k_1 = -0.9097$ and $k_2 = 15.8687$. Maximum CEX ion volumetric production rates for xenon thruster conditions mentioned previously are around 10^{20} m^{-3} s^{-1}.

Volumetric CEX production rates using Eq. (12) in the plume of a 12-mN (thrust) 15-cm (beam diameter) xenon ion thruster operating with a beam current of 0.23 A, a beam voltage of 1000 V, and a propellant utilization efficiency of 0.84 are shown in Fig. 2. Equation (5) was used for the beam ion density, and the neutral density was given by Eq. (10). Overlaid on the computed values are those based on measurements.[13] It was noted in the experiment that the integral of the measured beam ion current density over the thruster exit, which should be equal to the total beam current, was smaller by 15%. Therefore, we have reduced our values 15% for comparison. The CEX production rates agree well.

There is a limit to the validity of this method for computing the CEX ion creation. If the CEX ion production rate is too high, the beam ion and neutral densities cannot be taken to be constant. Defining a CEX ion current to be the current produced

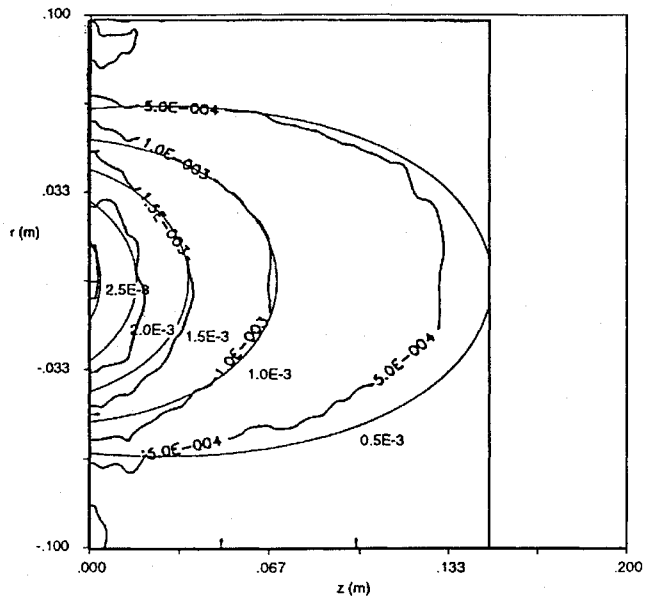

Fig. 2 Comparison of xenon CEX ion production rates with data.[13] Two-dimensional ion thruster plume simulation; CEX production rate (mA/cm^3) reduced 15% for comparison.

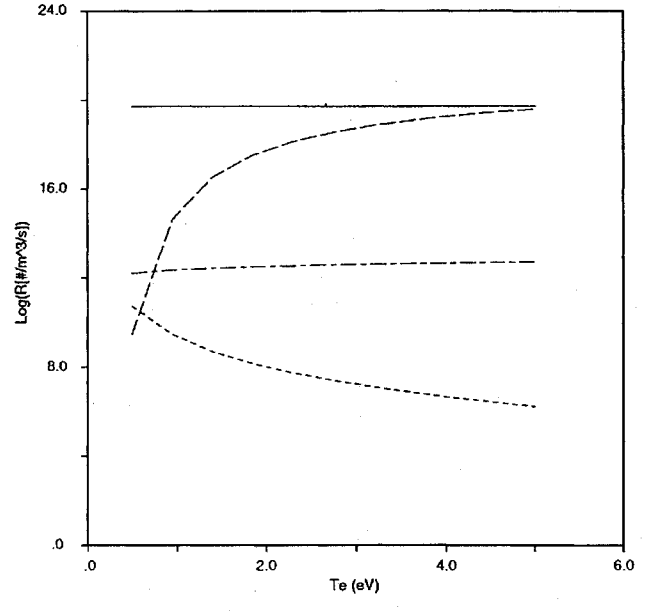

Fig. 3 CEX, ionization, and recombination rates of Xe vs electron temperature. Two-dimensional ion thruster plume simulation; comparison of CEX, ionization (1st), and recombination rates for Xe: ——, CEX; – – –, ionization; - - - -, three-body recombination; and – – –, radiative recombination.

within a sphere of radius r_T (using maximum parameters), $I_{\text{cex}} = \frac{4}{3}\pi r_T^3 e n_{n0} n_{bi0} v_{bi} \sigma_{\text{cex}}(v_{bi})$, the ratio of I_{cex} to the beam current $I_b \approx e n_{bi0} v_{bi} \pi r_T^2$ must be small, i.e., $I_{\text{cex}}/I_b \sim r_T n_{n0} \sigma_{\text{cex}} \ll 1$. Typically this ratio, which is also the ratio of the thruster radius to the CEX collisional mean free path, is less than 10%.

In addition to CEX, other mechanisms of production as well as depletion of ions take place in the beam. Electron impact ionization was examined using the model of Drawin.[15] For recombination, there are two main types considered: the three-body Hinnov–Hirschberg model[15] ($i + e + e \rightarrow n + e$) and radiative recombination ($i + e \rightarrow n + h\nu$). Figure 3 shows a comparison of volumetric rates for CEX, ionization (single), and three-body and radiative recombination as a function of electron temperature for xenon. The beam ion and neutral density values have been listed above. For electron temperatures up to 3 eV, CEX is the dominant ion creation mechanism; beyond 5 eV, ionization becomes dominant. Compared to ion creation processes, recombination is negligible in the beam. Since most current ion thrusters operate with electron temperatures close to 1–2 eV, we will only include CEX processes in our model.

An important consideration for the transport of the slow CEX ions is the ambient and thruster-induced magnetic fields. A thermal (500 K) CEX ion has a gyroradius of about 10 m in low Earth orbit (LEO) and 2 km in geosynchronous Earth orbit (GEO), whereas the beam ions have gyroradii on the order of hundreds of meters in LEO, and hundreds of kilometers in GEO. Thus, for the length scales that we are interested in currently (<2–5 m), the ions can be considered unmagnetized with respect to the ambient magnetic field. Ion thrusters also have magnetic fields surrounding them due to the magnets inside the thruster that serve to confine primary electrons to increase their ionization efficiency. Modern ion thrusters use ring-cusp magnetic fields,[16] which are localized within the chamber, and hence the effect of external thruster magnetic fields in the plume is not modeled.

NPE

The presence of sputtered grid metal in the plume presents a serious contamination hazard due to these species' low vapor pressures. Currently, molybdenum is the most common grid metal, although carbon–carbon composite grids show much promise due to their high sputter resistance.[17] For this work, we only consider two-grid molybdenum systems. Ground experiments[18–20] and computational modeling,[21] have shown that sputtering by propellant CEX ions occurs within the aperture holes and on both the upstream and downstream faces of the accelerator grid because of its negative bias. However, the downstream face is eroded the most. The sputtered molybdenum is ejected as neutral atoms, since the ionization energy, 7.1 eV, is greater than the work function, 4.6 eV. A fraction of the neutral molybdenum becomes ionized, either by CEX or by electron impact, depending on the electron temperature.

NPE ion densities are much less than those of the propellant CEX ions, and thus the perturbative effect of NPE ions on the self-consistent potential structures in the plume is negligible. Hence, given an NPE production model, one can use the potential fields computed self-consistently from the beam and propellant CEX ions, and then track the NPE ions in this field. This approach will be valid as long as the NPE ion density remains much smaller than the plasma density from which the potentials were calculated.

There are a number of approaches to computing the flux of neutral sputtered grid material. One is to use the measured grid impingement current to determine the sputtering rate.[22] However, this approach will overestimate the amount of sputtered material downstream in the plume, since the sputtered grid metal is not all ejected in the downstream direction, but can redeposit on other areas of the grids. Another approach is to use the grid mass loss M measured over a period of time t and define the average flux as

$$\Gamma_s = (M/tA_g)(\mathcal{N}_A)/(\mathcal{M}) \tag{14}$$

This approach will give an average erosion rate, since erosion varies as a function of time.

There are two important issues to address concerning the sputtered molybdenum neutrals: their sputtering distribution and their energy distribution. If the average velocity of the sputtered atoms is known, the average density at the surface can be computed, and by knowing the sputtering distribution, a density map can be constructed. Unfortunately, the energy distribution of molybdenum atoms sputtered by xenon ions apparently has not been measured, but data exist for bombardment by krypton at energies of 1200 eV (Ref. 23). The energy distributions for sputtering of copper by xenon and krypton at 600 eV are very similar, so we will use the krypton data.[24]

The energy distribution of the sputtered atoms is found to resemble a Maxwellian distribution, although the energetic tail is broader. The most probable ejection energy of molybdenum being bombarded by 1200-eV krypton ions is about 5 eV (3170 m/s), and the average energy is about 21 eV (6500 m/s); see Ref. 23. We model this energy distribution simply as a Maxwellian distribution,

$$F(E) \sim E \exp(-E/E_{\text{mp}}) \tag{15}$$

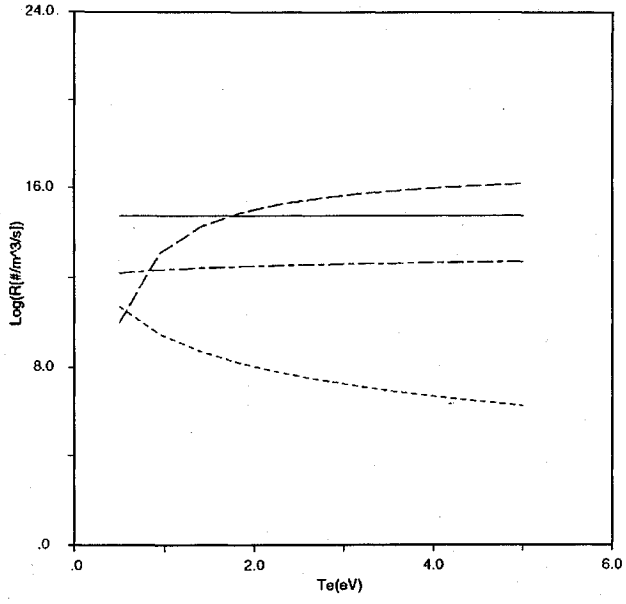

Fig. 4 CEX, ionization, and recombination rates of Mo vs electron temperature. Two-dimensional ion thruster plume simulation; comparison of CEX, ionization (1st), and recombination rates for Mo: ——, CEX; – – –, ionization; - - -, three-body recombination; and – - –, radiative recombination.

Although using a simple Maxwellian distribution does not capture the broader energetic tail, its use is conservative, since lower-energy ions will be influenced more by the electric potentials in the plume. As an example, computational modeling for a 30-cm xenon thruster, at an operating condition with a beam current of 3.2 A and an accelerator-grid bias of −331 V, predicted space operational values of a 3.73-g grid mass loss in 890 h (Ref. 21). Taking the grid area A_g to be simply πr_T^2, we obtain from Eq. (14) a flux of 1.03×10^{17} m^{-2} s^{-1}. Dividing the above flux value by the most probable ejection velocity, 3170 m/s, we obtain a density of 3.25×10^{13} m^{-3}, which is about four orders of magnitude less than the neutral propellant density.

Sputtering from monocrystalline metal surfaces usually exhibits preferred directions of ejection due to the crystallographic orientations. However, for a polycrystalline surface, the crystal surfaces are randomly oriented, and the sputtered distribution has generally been modeled as a cosine distribution.[25] We assume that the neutral sputtered molybdenum distribution downstream of the thruster is very similar to the propellant neutral distribution, i.e., a cosine distribution that falls off as $1/R^2$, and use Eq. (10) to describe the neutral molybdenum density distribution in the plume.

Lastly, there are two possible mechanisms we consider for molybdenum ion creation: CEX with the propellant ions, and electron impact ionization. The CEX cross section between xenon and molybdenum[26] for the energy range of interest (0.1–10 keV) is nearly constant, with a value around 6×10^{-20} m^2. Figure 4 shows a comparison of volumetric rates of CEX, electron impact ionization (single), and three-body and radiative recombination as a function of electron temperature for molybdenum. For maximum estimates, the relative collision velocity for the CEX rates is taken to be the beam ion velocity, and the beam ion density previously listed is used. The molybdenum neutral density used is 3.25×10^{13} m^{-3}. We can see that at lower electron temperatures near and below 1 eV, CEX is dominant. However, at temperatures beyond 1.75–2 eV, electron impact ionization is the dominant ion production mechanism, because of molybdenum's low ionization energy of 7.1 eV.

Electrons

Electrons from the neutralizer and the ambient plasma play a vital role in ion-thruster operation by neutralizing the ion beam. Essentially, the neutralizer produces a quasineutral plasma cloud that acts as a bridge for the passage of electrons to the beam. In ion-thruster beam plasmas, the thermal velocity of the electrons (T_e = 1–5 eV, velocity 4×10^5–9×10^5 m/s) is much higher than the ion beam velocity (2–4 $\times 10^4$ m/s), and thus the electrons can diffuse rapidly to provide neutralization. It is beyond the scope of this work to include a detailed model of the physics of an electron-emitting hollow cathode, which is still not completely understood today. Ambient electrons also provide paths for current closure and beam neutralization, and the three-dimensional nature of current coupling in plasma clouds has been examined, but at length scales (kilometers) much greater than those of interest here.[27] The electrons in our model are those that are emitted from the neutralizer and rapidly spread throughout the plume and backflow regions to provide charge neutralization. The neutralizer electrons dominate the neutralization process within the length scales of interest, since their density is orders of magnitude greater than that of the ambient electrons in the vicinity of the spacecraft.

Electron Momentum Equation

The general momentum balance for the electrons, including electric ($\boldsymbol{E}$) and magnetic fields ($\boldsymbol{B}$), pressure forces, and collisional drag terms, is

$$\frac{\partial \boldsymbol{v}_e}{\partial t} + \boldsymbol{v}_e \cdot \nabla \boldsymbol{v}_e = -\frac{e}{m_e}(\boldsymbol{E} + \boldsymbol{v}_e \times \boldsymbol{B}) - \frac{\nabla p_e}{m_e n_e} + \boldsymbol{R}_e \qquad (16)$$

A scaling analysis of the momentum equation leads to insight and significant simplification. The accelerations in Eq. (16) have the following scalings:

Unsteady	Inertia	Lorentz	Pressure	Collisional drag
V/τ	V^2/L	$(eE/m) + \omega_{ce}V$	v_{te}^2/L	νV

Because we are interested in the motion of the CEX ions, the time scales involved are much larger than electron time scales. Thus, the electron unsteady and inertia terms can be neglected.

The ratio of the electric to magnetic components in the Lorentz acceleration term is $\Delta\phi/VBL$. To approximate this ratio, it is necessary to have an estimate for the electron drift velocity. Physically, the electrons can not overexpand the ions expanding in the plume, since a large charge imbalance would result. Therefore, the electron drift velocity at most must be on the order of the ion drift velocities, even though the electron thermal velocities are much higher. The expansion process in the radial direction is largely driven by the radial beam potentials, which accelerate the ions while retarding the electrons from overexpanding (similarly to an ambipolar diffusion process). In the axial direction, the electron thermal velocity exceeds the beam ion velocity by at least a factor of 10, but one would expect the electrons to drift along with the ions. Thus, as an estimate for the electron drift velocity, we use the beam ion velocity as an upper-bound order of magnitude. Numerically, the ratio of electric to magnetic forces then becomes at least 10^2 taking V to be on the order of the beam ion velocity and using magnetic field strengths of 2×10^{-5} T in LEO and 1×10^{-7} T in GEO. Hence, magnetic field effects are negligible compared to electric field effects.

Last, we examine the importance of the collisional drag terms compared to the remaining electric field and pressure gradient terms. The electron–ion collision frequency is taken to be given by the classical formula[15]

$$\nu_{ei} = 3.6 \times 10^{-6} \frac{n_i \ell n \Lambda}{T_e^{\frac{3}{2}}} \qquad (17)$$

Instabilities and plasma turbulence within the beam may result in anomalous electron–ion collisions. However, it remains for these mechanisms and their importance to be quantified. The electron–neutral collision frequency is given by

$$\nu_{en} = n_n \sqrt{(8kT_e/\pi m_e)}\sigma_{en} \qquad (18)$$

The ratio ν_{ei}/ν_{en} is a strong function of the electron temperature, being >10 for T_e = 1 eV, and <0.1 for T_e = 5 eV. However, the total electron collision frequency ($\nu_e = \nu_{ei} + \nu_{en}$) is on the order of 10^5 s^{-1} in the beam over the temperature range of 1–5 eV. With collision frequencies of this order, and our estimates of the electron drift velocity, the collisional drag terms are several orders

of magnitude less than both the electric field and pressure gradient terms.

As a result of the above scaling analysis, the electron momentum equation (16) reduces to a balance between the pressure and electric potential gradients,

$$e\nabla\phi = \frac{k\nabla n_e T_e}{n_e} \tag{19}$$

If the electron temperature is constant, Eq. (19) can be integrated to yield the isothermal Boltzmann relation $n_e \sim \exp(e\phi/kT_e)$. However, as seen in experiments, the electron temperature decreases radially and axially because of cooling as the plume expands. The variation of the electron temperature, however, is much less than that of the plasma density on account of the high electron thermal conductivity: $(1/L)\Delta T_e/T_e \ll (1/L)\Delta n_e/n_e$ (Ref. 9). Hence, a first-order solution to Eq. (19) yields a Boltzmann relationship with a spatially varying temperature,

$$n_e(\boldsymbol{x}) = n_{e\infty} \exp\left[\frac{e\phi(\boldsymbol{x})}{kT_e(\boldsymbol{x})}\right] \tag{20}$$

where the electron density is a specified background density, denoted by subscript ∞, when the potential far from the beam falls to zero. The use of the reference point in the far field does not imply that the electrons described by Eq. (20) are from the ambient; rather, it serves as a far-field boundary condition to ensure quasineutrality. The positive potentials in the beam may be attracting ambient electrons, but their contribution to the neutralization process is insignificant in the near field. Indeed, the accelerating ambient electrons attracted by the positive beam potential are not properly described by a Boltzmann relationship, since they cannot be in equilibrium. However, for the neutralizer electrons, the positive beam potential provides a retarding force so that they do not abandon the ions as they expand, creating a large charge imbalance. The Boltzmann relationship simply states that these electrons are restrained in a condition where the electric field balances the pressure. It is important to stress that the multiple-scales argument is based on experimental observations, and that data suggest the plausibility of a Boltzmann relationship for the electrons.[9] It is checked a posteriori that indeed, temperature gradients are less than density gradients as well as potential gradients, which are large—particularly at the beam edge. Recently, preliminary efforts have been made to model the electrons kinetically, which will provide a more complete picture of electron behavior, particularly aspects of the drift velocities.[28]

Electron Temperature Equation

The electron temperature is given by the general electron energy equation

$$\frac{3}{2}n_e\left(\frac{\partial}{\partial t} + \boldsymbol{v}_e\cdot\nabla\right)kT_e + p_e\nabla\cdot\boldsymbol{v}_e = -\nabla\cdot\boldsymbol{q}_e + Q_e \tag{21}$$

where $\boldsymbol{q}_e = -\kappa_e\nabla T_e$ is the conductive heat flux. For the electron heating–cooling term Q_e, we consider collisional transfer and ohmic heating,

$$Q_e = -3(m_e/m_i)\nu_e n_e k(T_e - T_H) + \boldsymbol{j}_e\cdot\boldsymbol{E} \tag{22}$$

where the heavy-species temperature T_H of the ions and neutrals is taken to be a constant corresponding to the temperature of the thruster chamber walls. The electron velocity $\boldsymbol{v}_e$ is taken to be the beam ion velocity in the beam, and zero outside. The electron thermal conductivity is given by[15]

$$\kappa_e = \frac{2.4}{1 + \nu_{ei}/\sqrt{2}\nu_e}\frac{k^2 n_e T_e}{m_e\nu_e} \tag{23}$$

At 5 eV, κ_e is on the order of 0.5 W/m K, whereas at 1 eV it is about 0.1 W/m K.

It is useful to also conduct a scaling analysis of Eq. (21). We take the electron pressure to be given by $p_e = n_e kT_e$, and neglect the unsteady term, because we are interested in the steady-state behavior:

Convection	Conduction	Collisional transfer	Ohmic
$\frac{Vp_e}{L}$	$\frac{v_{te}^2 p_e}{\nu L^2}$	$\frac{m_e}{m_i}\nu p_e$	$en_e V\frac{\Delta\phi}{L}$

Within the beam, the convection and ohmic terms play a role (with convection being comparable to the ohmic term), but they are weak compared to the conduction term, which is dominant throughout the plume (on account of the v_{te}^2 scaling). Collisional transfer is also weak compared to conduction, because of the electron–ion mass-ratio factor. Thus, the electron temperature equation basically represents a conductive heat transfer problem with weak sink terms. However, since the convective terms pose no computational difficulties, we include them for completeness. In addition, it should be noted that the heavy-species temperature will actually rise because of collisional heating by the electrons. However, since the collisional transfer term is weak, the assumption of isothermal ions and neutrals has little effect.

Numerical Model

To model the expansion of an ion-thruster plume, we employ the hybrid electrostatic plasma particle-in-cell (PIC) method.[29] In the electrostatic PIC technique, ions and electrons in a plasma are treated as macroparticles, where each macroparticle represents many actual particles. The charge of the simulation particles is deposited onto a grid, and a charge density is computed. From this density, Poisson's equation for the electrostatic potential is solved, and the particles are moved under the influence of this self-consistent electric field. A major shortcoming of explicit fully kinetic PIC codes, where electrons are treated as particles, is the very small time step that is required to resolve the electron motion. Since we are interested in the ion motion, we adopt the hybrid approach where the ions are treated as particles, but the electrons are treated as a fluid. In this manner, the time step is now on the ion time scale, which for Xe ions is about 490 times larger than the electron time scale.

The equation of motion of each ion macroparticle is integrated:

$$\frac{d\boldsymbol{v}_i}{dt} = \left(\frac{q}{m}\right)_i(\boldsymbol{E} + \boldsymbol{v}_i\times\boldsymbol{B}) \tag{24}$$

where, in the electrostatic approximation, $\boldsymbol{E} = -\nabla\phi$ and the potential is determined from Poisson's equation:

$$\nabla^2\phi = \frac{e}{\varepsilon_0}\left(n_e - \sum_{\text{species}} n_i\right) \tag{25}$$

Note that the summation over the ion species allows different species such as propellant and nonpropellant ions. In our simulation model, the slow CEX ions are treated as particles, with the ratio of real particles to macroparticles around 10^7 or more.

Our model is two dimensional (axisymmetric). Figure 5 shows a representative computational grid, which is nonuniform so as to more efficiently handle the highly nonuniform density distribution in the plume. Since the grid cell size should be on the order of the Debye length, we have stretched the grids in the r direction to follow the increase in Debye length away from the centerline due to the density decrease.

With the Boltzmann distribution for the electron density, the Poisson equation for the electric potential becomes nonlinear. This equation is solved with a Newton–Raphson successive-over-relaxation scheme. Fixed potentials are imposed on the spacecraft surfaces, usually around $-kT_e/e$, and the thruster front (the accelerator grid) is fixed at the accelerator-grid potential, usually -100 to -200 V. Neumann boundary conditions are imposed on all exterior boundaries.

The nonlinear electron temperature equation (21) is an advection–diffusion equation that is solved using a generalized minimal residual method with an incomplete Cholesky preconditioner as implemented in a numerical package, ITPACK.[30] The thruster front is set to a specified temperature, and the rest of the spacecraft surfaces are insulated. Neumann conditions are set at the upstream

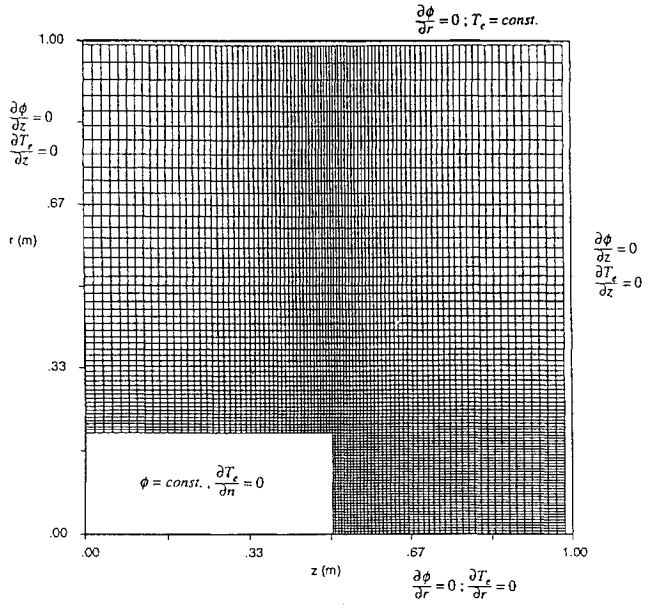

Fig. 5 Computational domain.

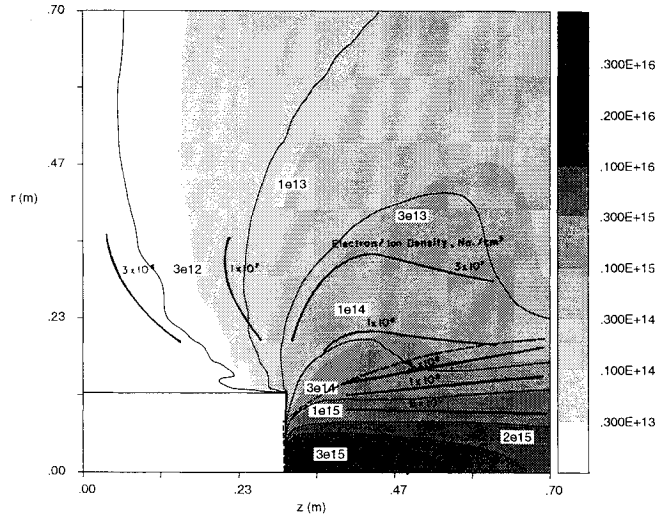

Fig. 6 Contour plot of total ion density compared with data.[9] Two-dimensional ion thruster plume simulation total ion density (m^{-3}).

and downstream boundaries, and the far radial boundary is set to a temperature based on a far-field temperature model.[7]

Because the temperature equation and Poisson's equation are coupled through the electron densities, it is necessary, for a given ion density, to iterate between the two equations until convergence is reached. The general structure of the solution process is outlined as follows. First the ion beam and neutral densities are computed on the grid, and the number of PIC CEX ions (either propellant or NPE) to be created in each grid cell is determined from the respective production rates. The velocities of the propellant CEX ions are drawn from a Maxwellian distribution with a temperature corresponding to the thruster wall, and the NPE ion velocities are taken from the ejected energy distribution given by Eq. (15). The particles are then weighted to the grid to compute the charge density. Given the total ion density that includes the beam ion density, the CEX ion density, and a uniform background density, Poisson's equation is solved for the electric potential. The electron density is based on a temperature from the previous time step (or at $t = 0$, an initial estimate). Based on the new potential and the previous temperature, the electron density can be computed for the collision frequency and thermal conductivity from Eq. (20). The electron temperature equation (21) is then solved, given coefficients that are based on the previous temperature, for a new temperature. This new temperature is fed back to Poisson's equation, where it appears in the Boltzmann relation for the electron density, and a new potential computed. Once the Poisson equation and the temperature equation have converged, the new self-consistent potential is used to compute the electric field under which the particles are moved. Particles that reach the simulation boundaries and spacecraft surfaces are removed. New particles are then created, new densities are computed at $t = t + 1$, and the process is repeated until steady state.

Results

In this section, simulation results are compared with data and the underlying physical mechanisms of the plume expansion are shown. Results shown here pertain to the propellant CEX plasma; those on sputtered molybdenum are shown in a companion paper.[8] The numerical model is run until steady state is reached, when the number of particles in the simulation reaches a constant value that is determined when the production rate of particles in the plume balances the loss rate at the exterior domain boundaries. Numerical results were checked for energy conservation and for independence of domain size and number of particles.[7]

Ion Density

Kaufman[9] investigated the propellant CEX plasma produced by a 15-cm SERT II thruster operating with mercury as the propellant and dished grids that permitted higher beam currents than the original flat grids that were used in the 1970 space flight. The screen and accelerator potentials were maintained at +1000 and −500 V, respectively, throughout the investigation, yielding an ion beam velocity of 31,011 m/s. The thruster was operated at two operating conditions: case A, $I_b = 0.63$ A, $\eta_p = 0.85$, and case B, $I_b = 0.38$ A, $\eta_p = 0.51$. The ground tests were conducted in a tank that was 1.2 m in diameter and 4.6 m long. However, the thruster exit was apparently only 30 cm from the back tank wall, and the proximity of the chamber wall may have influenced plasma properties in the backflow region. A neutral background pressure around 5×10^{-6} torr was maintained during thruster operation. The experimental error of measurements was assessed to be ±20–50%.

An examination of radial density profiles through the beam of this particular SERT II thruster showed that the beam ion density was better described by a Gaussian radial profile than by a parabolic profile. Thus, Eq. (6) was used to model the beam ion density. Based on measurements of the beam ion density, a 15-deg beam divergence angle was used, although it was never directly measured in the experiment. In comparing numerical results with data, both variable- and constant-electron-temperature results are shown. Kaufman measured the electron temperature at the thruster exit to be 5 eV. Thus, this value is a boundary condition for the variable-temperature model, and the constant-temperature model is held at 5 eV.

A contour map of the total ion density for the high-current case A is shown in Fig. 6. Overlaid are variable-temperature results (gray scale), constant-temperature ($T_e = 5$ eV) results (thin contours), and experimental data (bold contours in cgs units). Qualitatively, the agreement is quite good. Note that noticeable deviations between model and data take place in the beam; the plasma density measured within the beam is higher. The differences may well be due to the fact that ionization is important with mercury at electron temperatures above 4 eV. However, we are interested in the plasma densities outside the beam, and we can see that agreement is reasonably good, with constant-temperature results yielding larger densities in the backflow region. It must be kept in mind that these experimental contours have up to a 50% error associated with them. Even though calculations with a constant temperature do not accurately reflect all the physical processes in the plume, if the backflow density is close to, or gives an upper bound to, values obtained with the full temperature model, the reduced computational burden allows the constant-temperature model to be more efficient for parametric studies.

In Fig. 6, it is shown that the total ion density (beam and CEX) falls from values of 3–5 $\times 10^{15}$ m^{-3} in the beam to around 3×10^{12} m^{-3} at 30 cm behind the thruster exit plane—a three-order-of-magnitude decrease. In the beam, the beam ion plasma dominates; however, the CEX plasma still is on the order of 10^{15} m^{-3}, whereas outside the plume, the beam ion density is zero, and the CEX plasma is

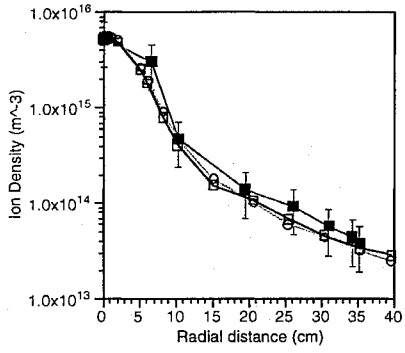

Fig. 7 Total ion density along radial cut through beam compared with data[9]: ■, data[9]; ○, model (var. T_e); and □, model (const T_e). 15-cm Hg SERT II; I_b = 0.63 A, η_p = 0.85, axial location: 13 cm downstream.

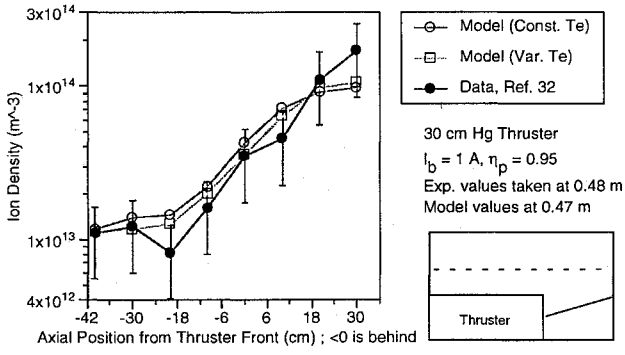

Fig. 8 Comparison of total ion density in backflow region with data.[32]

the sole component. In these simulations, the background plasma density is 10^{12} m^{-3}, a value inferred from the Boltzmann relationship and experimental measurements of the beam potential.

Figure 7 shows a radial cut of the total ion density through the plume at an axial location 13 cm downstream from the thruster operating with conditions of case A. Both constant- and variable-temperature simulation results are shown, and they are very similar, with the constant temperature giving slightly higher densities farther from the plume centerline. The total ion density falls from about 5×10^{15} m^{-3} at the beam centerline to below 10^{13} m^{-3} at 70 cm away. With ±50% error bars on the data, we see that the numerical results are in good agreement.

The propellant CEX flowfield of a 30-cm-beam-diameter 900-series Hughes mercury ion thruster using small-hole accelerator-grid optics was investigated in two different experiments.[31,32] The main objective of these experiments was to determine the flow angle of the CEX plasma with the end effect of a Langmuir probe, which is the phenomenon that the current collected by a Langmuir probe aligned with a flowing plasma is greater than if the probe is oriented at some other angle to the flow direction.

The 30-cm mercury thruster was operated over a range of beam currents ranging from 1 to 1.8 A in the first experiment, and it was found that the CEX plasma flow angle was insensitive to the beam current. In the second experiment, the thruster was run at a fixed operating point of 1 A with a propellant utilization efficiency of 0.95. The screen potential of the thruster was fixed at 1100 V, yielding a beam ion velocity of 32,525 m/s. Both experiments were conducted within a vacuum chamber 2.1 m in diameter and 4.6 m long. The tank background pressure ranged from 1×10^{-6} to 6×10^{-6} torr. In our simulations, a background pressure of 3.5×10^{-6} torr with a temperature of 300 K is used. No beam ion density profiles were measured in the experiments to suggest what type of profile to use (parabolic, Gaussian, or other). However, in view of similarities with the modern 30-cm Hughes thruster, a parabolic radial profile for the beam ions was used. From other measurements,[33] the electron temperature in the beam ranged from 0.2 to 1 eV; thus the electron temperature at the thruster exit was fixed at 1 eV.

In the experiments in Ref. 32, the plasma density at a radial distance of 48 cm was measured from 30 cm in front of the thruster to about 40 cm behind the thruster. Figure 8 shows the data points,

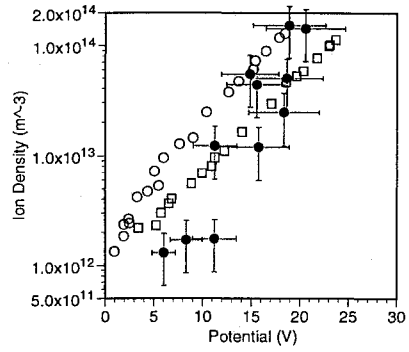

Fig. 9 Total ion density vs potential: simulation results and data[9]: •, data[9]; □, model (const T_e); and ○, model (var. T_e). 15-cm Hg SERT II, I_b = 0.63 A, η_p = 0.85.

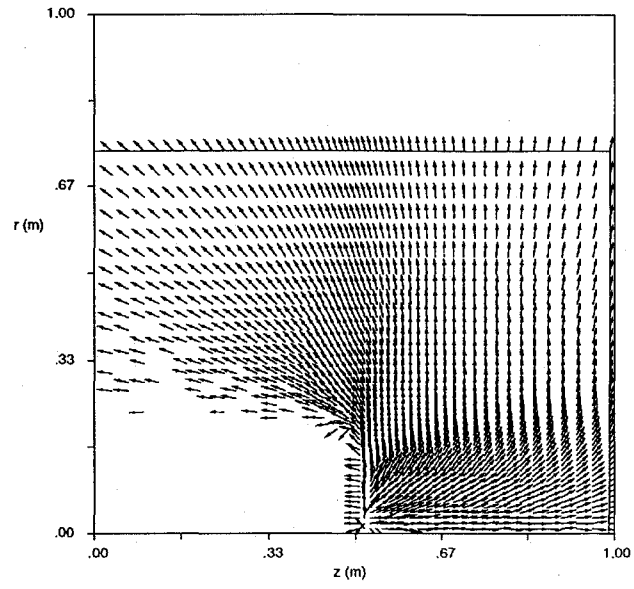

Fig. 10 Vector map of CEX ion flow angle for thruster in Ref. 31. Two-dimensional ion thruster plume simulation; CEX flow vectors (normalized).

along with model calculations at r = 47 cm for both variable- and constant-temperature models. It can be seen that there is very good agreement between model and experiment, with the constant-temperature model giving slightly higher values again. Based on the experimental measurements, a uniform plasma background of 10^{13} m^{-3} was imposed in the simulations. Note that the experiments in Refs. 31 and 32 were held in a tank with diameter about twice that for the other experiments,[9] and hence one expects reduced test-chamber effects.

Plasma Potential and Electron Temperature

Figure 9 shows potential and density data from a Langmuir probe in the plume of the 15-cm SERT II thruster taken by Kaufman (operating conditions A).[9] Error bars corresponding to ±20% in potential and ±50% in density have been added to the experimental data, which have considerable scatter. Overlaid are both the isothermal and variable-temperature model results. For higher potentials, corresponding to the beam ion density, the numerical results fall within the error bars of the experimental data, with the isothermal model yielding lower density values for a given potential. However, at lower densities, corresponding to the CEX plasma, the numerical values of the corresponding potentials are much lower, suggesting that in ground experiments the presence of the facility walls may play an important role in the potential distribution and (perhaps to a certain degree) the electron temperature. Because of the negative bias on the walls, the electrons from the thruster are repelled, and it is quite likely that secondary electron emission from the tank walls occurs, which may alter the temperature near the walls.

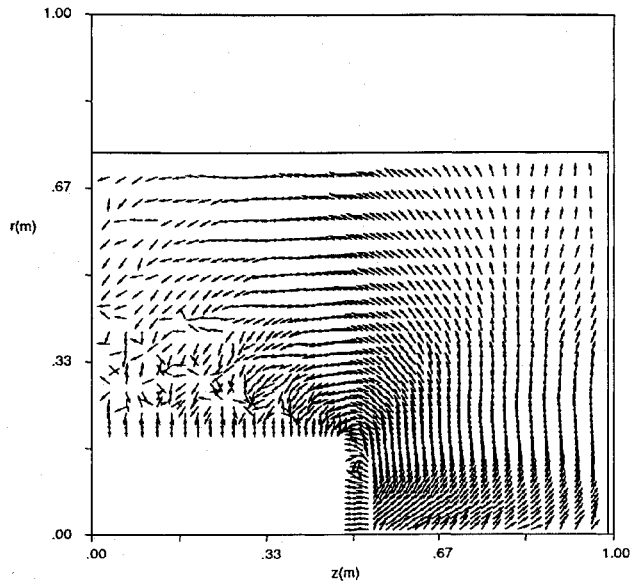

Fig. 11 Vector map of electric field for thruster in Ref. 31. Two-dimensional ion thruster plume simulation, electric field vectors (normalized).

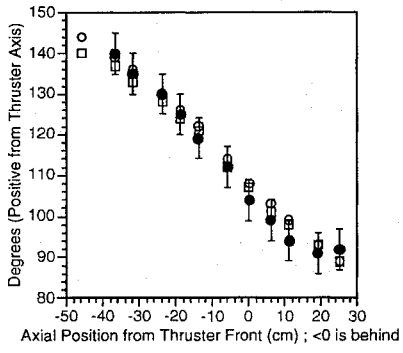

Fig. 12 Comparison of CEX ion flow angle with data[31]: ○, model (const. T_e); □, model (var. T_e); and •, data[31]. 30-cm Hg thruster, I_b = 1 A, η_p = 0.95; experimental values taken at 0.66 m, model values at 0.65 m.

The electron temperature can be deduced from Fig. 9 by taking the slope of a plot of the natural ‹garithm of the ion density vs the potential. A least-squares fit through Kaufman's data yields a temperature of 3 eV. For the variable-temperature results, two temperatures can be deduced: one from the beam plasma (higher density and potential), and one for the CEX plasma (lower density and potential). The corresponding temperatures are 5 and 2.6 eV. The computed temperature of the CEX plasma is close to what was observed.[9] The electron temperature actually plays an important role in the magnitude of the backflowing current, since potentials scale with T_e. In a companion paper, the sensitivity of the backflow current to the electron temperature is examined.[8]

Plasma Flow Angle

Based on the CEX ion velocities, CEX plasma flow direction vectors can be mapped out. Figure 10 shows the computed CEX ion current-density vector flowfield, with the vectors normalized so that only direction is indicated, and not magnitude. CEX ions that are created in the beam near the centerline do not see a strong radial electric field, and hence they are carried downstream by the axial potential gradient in the beam. However, as they move farther out radially in the beam, the radial potential gradient starts to turn the CEX ions towards the beam edge, and as shown in Fig. 10, the CEX ions that reach the beam edge leave completely radially. Outside of the beam, at and behind the thruster exit plane, the electric fields turn the CEX ions towards the backflow direction. Also, it can be seen that CEX ions that are close to the top edge of the thruster body are turned back the most, and some are even pulled down toward the thruster-body top. In addition, CEX ions are shown to be directly attracted back to the negatively biased accelerator grid, which constitutes the grid impingement current.

Figure 11 shows a vector plot of the electric field, normalized so that only direction is indicated. A comparison of Figs. 10 and 11 clearly shows how the CEX ions are influenced by the electric field. Note that the electric field is almost radial at the beam edge even though the beam is divergent, and is axial in the backflow direction 90 deg above the thruster exit. In addition, the electric fields in the sheaths surrounding the thruster body that serve to accelerate CEX ions to the surfaces can be seen. Above the thruster body for $z < 30$ cm, the electric field is noisy because of differencing of the potential, which is noisy because the CEX ion density is low in that region.

The CEX plasma flow angles[31] were measured at distances of 48 and 66 cm from the plume centerline. Measurements up to 51 cm in both the upstream and downstream directions were taken. The experimental error on measurements was assessed to be ±2–5 deg. We have performed simulations with both variable and isothermal

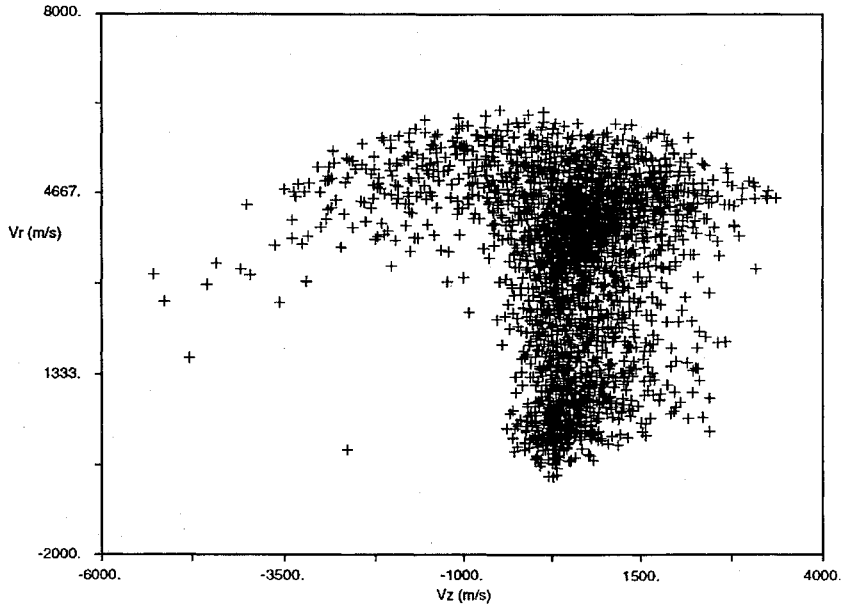

Fig. 13 Phase-space plot of CEX ions: radial vs axial velocity for thruster in Ref. 9. Two-dimensional ion thruster plume simulation, phase space plot (variable T_e).

models, and the computed flow angles are shown with experimental data in Fig. 12 for a radial distance of 65 cm. The simulation results shown are displaced 1 cm radially with respect to the experimental data because of the computational grid structure.

In the region behind the thruster exit in Fig. 12, which is of most concern for contamination, there is excellent agreement with experiment, with very slight difference between variable-temperature and isothermal results. Differences can be attributed to the fact that with the isothermal model, the CEX ions are turned back more by the stronger electric fields. This is indeed the case; flow angles with the isothermal model are slightly higher (~1–3 deg). We note that the smaller the radial distance to the plume, the greater the turning angle. The flow leaves at 90 deg to the plume axis at about 10–20 cm downstream of the thruster, which gives the appearance of a point source located about one thruster radius downstream. However, the flow that enters the backflow region leaves from the beam much closer to the thruster. These backflowing ions leave radially, and are then turned back by the electric fields—giving the appearance that they originated from a point farther downstream in the beam.

Last, it is of interest to examine a phase-space plot of the propellant CEX ions. In Fig. 13, a plot of the radial and axial velocities of mercury CEX ions from the Kaufman case A thruster is shown that clearly shows two different populations. There is a lower-energy population that is created within the beam with a thermal velocity distribution, and there is a high-energy population representing the CEX ions that have gained energy from being accelerated by the radial beam electric fields. The radial velocity of the energetic CEX population is around 4500 m/s, which is due to the radial beam potential drop of about 20 V. In addition, the energetic CEX ions have a backstreaming velocity component up to 3500 m/s. These ions constitute the backflow towards the spacecraft.

Conclusions

We have developed a physical and numerical model of the backflow contamination of an ion-thruster plume. Detailed models for all the thruster effluents and plume components, including the beam ions, neutral propellant, CEX propellant ions, sputtered grid ions, and neutralizing electrons, were developed and integrated into a comprehensive numerical model for axisymmetric geometry. Simulation results were compared with experimental data, and comparisons of ion density, electron potential and temperature, and CEX ion flow angle showed good agreement. However, these data are for mercury, an obsolete propellant. What is most important is a modern experimental effort to characterize the plume backflow of xenon thrusters by using modern diagnostic techniques to provide a complete database of the plume densities, current densities, electron temperatures, and potentials in the backflow regions that can be used to validate plume contamination models. These models will enable spacecraft designers and integrators to more confidently assess, and control if necessary, the contamination of EP thrusters and will thus help EP emerge as a commonly accepted form of spacecraft propulsion.

Acknowledgments

R.I.S.R. was supported in part by a National Science Foundation Graduate Fellowship. Support for R.I.S.R. and D.E.H. is also acknowledged from the U.S. Air Force Office of Scientific Research, the Jet Propulsion Laboratory of the California Institute of Technology, and the Applied Physics Laboratory (APL) of Johns Hopkins University. N.A.G. was supported by APL. The authors would like to acknowledge useful discussions with Manuel Martinez-Sanchez of the Massachusetts Institute of Technology and Barry Mauk of APL.

References

[1]Pollard, J. E., Jackson, D. E., Marvin, D. C., Jenkin, A. B., and Janson, S. W., "Electric Propulsion Flight Experience and Technology Readiness," AIAA Paper 93-2221, June 1993.

[2]Byers, D. C., "Electron Bombardment Thruster Field and Particle Interfaces," *Journal of Spacecraft and Rockets*, Vol. 16, No. 5, 1979, pp. 289–301.

[3]Deininger, W. D., "Electric Propulsion Produced Environments and Possible Interactions with the SP-100 Power System," AIAA Paper 85-2046, Sept. 1985.

[4]Carruth, M. R., "A Review of Studies on Ion Thruster Beam and Charge-Exchange Plasmas," AIAA Paper 82-1944, Nov. 1982.

[5]Komatsu, G. K., and Sellen, J. M., "Beam Efflux Measurements for a 30-cm Mercury Ion Thruster," AIAA Paper 76-1052, Nov. 1976.

[6]Robinson, R. S., Kaufman, H. R., and Winder, D. R., "Plasma Propagation Simulation Near an Electrically Propelled Spacecraft," *Journal of Spacecraft and Rockets*, Vol. 19, No. 5, 1982, pp. 445–450.

[7]Samanta Roy, R. I., "Numerical Simulation of Ion Thruster Plume Backflow for Spacecraft Contamination Assessment," Ph.D. Thesis, Dept. of Aeronautics and Astronautics, Massachusetts Inst. of Technology, Cambridge, MA, June 1995.

[8]Samanta Roy, R. I., Hastings, D. E., and Gatsonis, N. A., "Numerical Study of Spacecraft Contamination and Interactions by Ion-Thruster Effluents," *Journal of Spacecraft and Rockets*, Vol. 33, No. 4, 1996, pp. 535–542.

[9]Kaufman, H. R., "Charge-Exchange Plasma Generated by an Ion Thruster," NASA CR-134844, June 1975.

[10]Beattie, J. R., and Matossian, J. N., "High Power Ion Thruster Technology," NASA CR-187161, Feb. 1992.

[11]Bird, G. A., *Molecular Gas Dynamics*, 1st ed., Clarendon, Oxford, England, UK, 1976, p. 106.

[12]Staggs, J. F., Gula, W. P., and Kerslake, W. R., "Distribution of Neutral Atoms and Charge-Exchange Ions Downstream of an Ion Thruster," *Journal of Spacecraft and Rockets*, Vol. 5, No. 2, 1968, pp. 159–164.

[13]Monheiser, J. M., "Advanced Electric Propulsion Research—1990," NASA CR-187103, May 1991.

[14]Rapp, D., and Francis, W. E., "Charge Exchange Between Gaseous Ions and Atoms," *Journal of Chemical Physics*, Vol. 37, No. 11, 1962, pp. 2631–2645.

[15]Mitchner, M., and Kruger, C. H., Jr., *Partially Ionized Gases*, 1st ed., Wiley, New York, 1973, Chap. 2.

[16]Sovey, J., "Improved Ion Confinement Using a Ring-Cusp Ion Thruster," AIAA Paper 82-1928, Nov. 1982.

[17]Messerole, J. S., "Measurement of Relative Erosion Rates of Carbon–Carbon and Molybdenum Ion Optics," AIAA Paper 94-3119, June 1994.

[18]Rawlin, V., "Internal Erosion Rates of a 10-kW Xenon Ion Thruster," AIAA Paper 88-2912, July 1988.

[19]Patterson, M. J., and Verhey, T. R., "5 kW Xenon Ion Thruster Lifetest," AIAA Paper 90-2543, July 1990.

[20]Fearn, D. G., "Ion Thruster Lifetime Limitations Imposed by Sputtering Processes," International Electric Propulsion Conf., Monterey, CA, Paper 93-177, Sept. 1993.

[21]Peng, X., Ruyten, W., and Keefer, D., "Charge-Exchange Grid Erosion Study for Ground-Based and Space-Based Operations of Ion Thrusters," International Electric Propulsion Conf., Monterey, CA, Paper 93-173, Sept. 1993.

[22]Kaufman, H. R., and Carruth, M. R., "Charge-Exchange Plasma Environment for an Ion Drive Spacecraft," Jet Propulsion Lab., California Inst. of Technology, Publication 79-90, Pasadena, CA, Oct. 1981.

[23]Stuart, R. V., Wehner, G. K., and Anderson, G. S., "Energy Distribution of Atoms Sputtered from Polycrystalline Metals," *Journal of Applied Physics*, Vol. 40, No. 2, 1969, pp. 803–812.

[24]Stuart, R. V., and Wehner, G. K., "Energy Distribution of Sputtered Cu Atoms," *Journal of Applied Physics*, Vol. 35, No. 6, 1964, pp. 1819–1824.

[25]Weigand, A. J., and Mirtich, M. J., "Measurement of Sputtered Efflux from 5-, 8-, and 30-cm Diameter Mercury Ion Thrusters," AIAA Paper 75-358, March 1975.

[26]Rutherford, J. A., and Vroom, D. A., "Charge Transfer Cross Sections for Hg^+, Xe^+, and Cs^+ in Collision with Various Metals and Carbon," *Journal of Chemical Physics*, Vol. 74, No. 1, 1981, pp. 434–441.

[27]Gatsonis, N. A., and Hastings, D. E., "Evolution of the Plasma Environment Induced by Gas Releases from Spacecraft: Three-Dimensional Modelling," *Journal of Geophysical Research*, Vol. 97, No. 10, 1992, pp. 14,989–15,005.

[28]Wang, J., Brophy, J., Liewer, P., and Murphy, G., "Modeling Ion Thruster Plumes," AIAA Paper 95-0596, Jan. 1995.

[29]Birdsall, C. K., and Langdon, A. B., *Plasma Physics via Computer Simulation*, 2nd ed., Adam Hilger, Bristol, England, UK, 1991.

[30]Oppe, T. C., Joubert, W. D., and Kincaid, D. R., "A Package for Solving Large Sparse Linear Systems by Various Iterative Methods," Center for Numerical Analysis, Univ. of Texas, CNA-216, Austin, TX, April 1988.

[31]Carruth, M. R., and Brady, M. E., "Measurement of the Charge-Exchange Plasma Flow from an Ion Thruster," *Journal of Spacecraft and Rockets*, Vol. 18, No. 5, 1981, pp. 457–461.

[32]Carruth, M. R., Gabriel, S. B., and Kitamura, S., "Ion Thruster Charge-Exchange Plasma Flow," AIAA Paper 82-0403, Jan. 1982.

[33]Gabriel, S. B., and Kaufman, H. R., "A Comparison of Experimental and Computer Model Results on the Charge-Exchange Plasma Flow from a 30-cm Mercury Ion Thruster," AIAA Paper 82-1946, Nov. 1982.

I. D. Boyd
Associate Editor